

Modeling The Imaging Performance Of Ground-Based Telescopes

Richard H. Boucher, Edward J. Beiting, Kameron W. Rausch

The Aerospace Corporation, 2350 E. El Segundo Blvd, El Segundo CA USA 90245

Benjamin S. Wheeler, Lisandro Leon

Trex Enterprises, 10455 Pacific Center Court, San Diego CA USA 92121

ABSTRACT

Two independently-developed optical models were created to assess the feasibility of image-based attitude determination of a low-earth-orbit (LEO) satellite using a meter-class deployable telescope. Both models integrate existing AFRL tools for satellite modeling (TASAT) and atmospheric transmission and sky backgrounds (PLEXUS), with different turbulence, image-formation, and speckle-imaging post-processing algorithms. The end-to-end results of the two simulations were compared and found to agree very closely. The results to-date indicate that attitude determination using the best reconstructed images under moderate atmospheric conditions should be possible for a one-meter class telescope. However, images taken at less than ideal viewing angles or with more severe atmospheric conditions are not amenable to attitude determination using only post-processing algorithms.

1. INTRODUCTION

We have been conducting conceptual design work on a field-deployable meter-class telescope system. One of the primary missions will be to image a low-earth orbit (LEO) satellite during the daytime and near terminator to determine position and attitude along some portion of its orbit.

The telescope could be deployed in locations with poor seeing, such as in the desert during daytime with strong turbulent boundary layers. The goal of the simulation was to assess the feasibility of using a one meter-class telescope in locations with these harsh seeing conditions for imaging satellites during the daytime with post-processing in the absence of adaptive optics, and determine if the resulting image quality is sufficient to measure its attitude.

The prime contractor for the telescope conceptual design and integration is Trex Enterprises of San Diego CA and Maui HI. The Aerospace Corporation provides systems engineering and analysis support to the Air Force.

2. CONCEPTUAL DESIGN AND SYSTEM PARAMETERS

A point design was selected for the telescope as a starting point for the simulations. The telescope diameter is 1.2 meters, and the focal length was chosen to obtain Nyquist sampling for the visible and NIR focal plane cameras (which have 16 and 25 micron pixels respectively) at the center wavelengths of 0.8175 and 1.25 microns for each channel. The focal plane readout rate is 50 Hz, with a nominal 20 msec integration time, which would give some blurring of the speckled images due to atmosphere motion and telescope slew. We allow for the possibility of an adaptive optics deformable mirror and wavefront sensor in the design, although this was not used in the simulation since we assessed the feasibility of using post-processing only.

The telescope could be located in a high-desert area at an altitude of approximately 5000 feet, such as Kirtland AFB near Albuquerque, New Mexico. Fig. 1 is a schematic of the telescope concept, and a detailed listing of the parameters used in the simulation is in Table 1.

3. DESCRIPTION OF SIMULATION AND MODELS

Fig. 2 is a top-level block diagram showing the major software components: PLEXUS for atmosphere transmission and radiance, TASAT for orbit track and target radiance profile, followed by an optical imaging through turbulence model and image post-processing. Adaptive optics was not implemented for this phase of the study. The final step of determining the satellite attitude from the image, was also not done as part of this study; the images were qualitatively assessed. Fig. 3 is a more detailed block diagram flow of the atmospheric turbulence propagation model, optical imaging model, and speckle-imaging post-processing. These components are described in greater detail below.

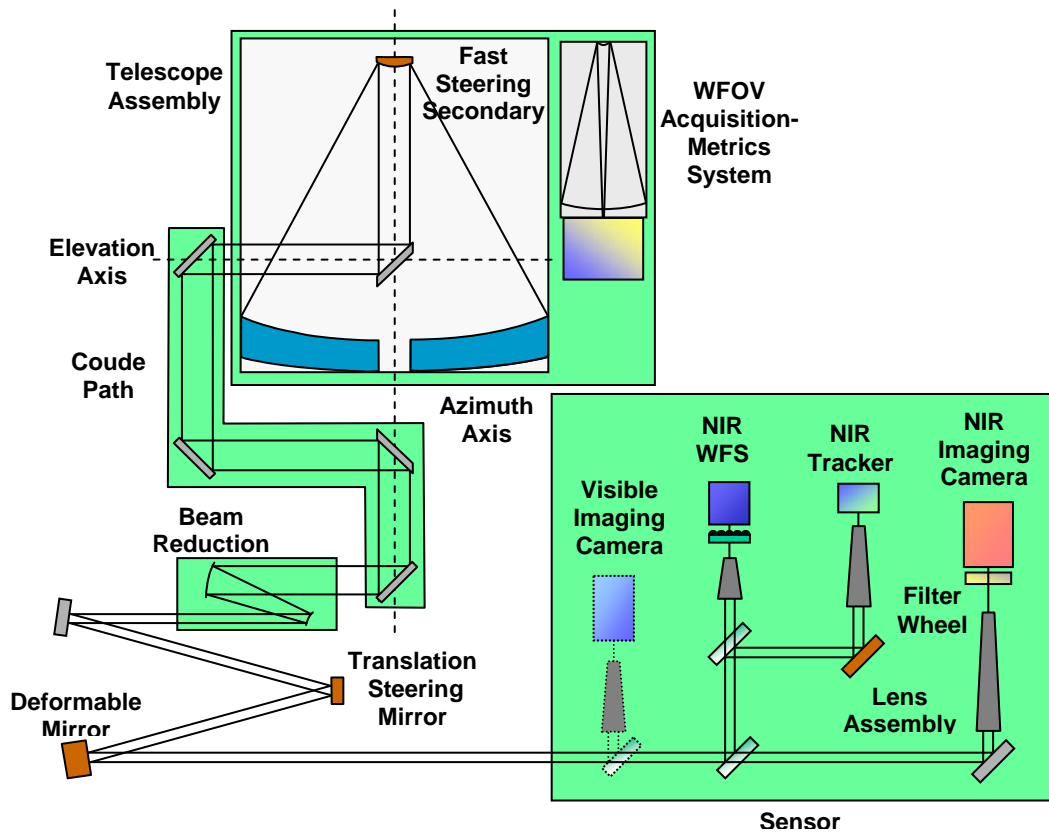


Fig. 1 Telescope concept

Table 1. Nominal Telescope system parameters used in simulation

Parameter	Visible channel	NIR channel
Location	Kirtland AFB	
Latitude/Longitude	35.0483 N 106.6067 W	
Altitude (ground/aperture)	1621 m / 1630 m	
Time/Date	10 AM local time, March 21	
Satellite model	HiFly, 1.5 m dia x 5 m	
Satellite zenith angle	45, 52, 60 deg (see Table 2)	
Slew rate	(see Table 2)	
Telescope diameter	1.2 m	
Obscuration diameter	0.11 m	
Atmosphere transmission	From PLEXUS (see Table 2)	
Atmosphere background	From PLEXUS (see Table 2)	
Atmosphere CN2 profile	Kirtland "Best", "Worst" (section 3.4)	
Effective Focal length	46.97 m	48.00 m
Bandpass	0.7 – 0.935 μm	1.12 – 1.38 μm
Optics Transmission	0.542	0.383
Static wavefront error	142 nm rms	144 nm rms
IFOV	0.34 μrad	0.52 μrad
Pixel size	16 μm	25 μm
Quantum Efficiency	(see Fig. 5)	(see Fig. 5)
FPA readout noise	1 e- rms	70 e- rms
Dark current	1 e-/pix/sec	6.4e4 e-/pix/sec
Integration time	20 msec	20 msec
Number of frames	100 (target) 200 (star)	

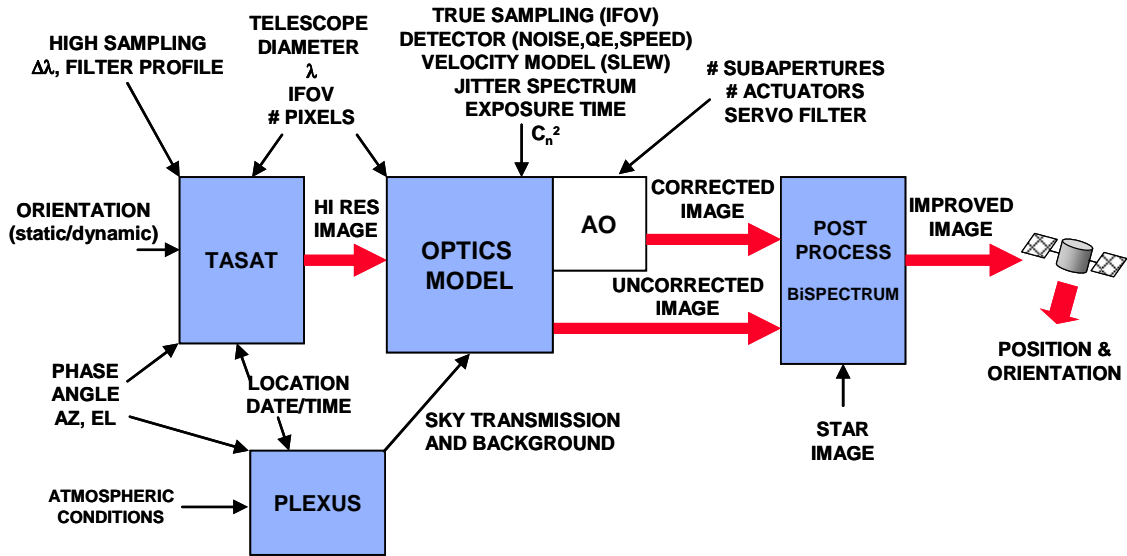


Fig. 2. Principal software modules of simulation

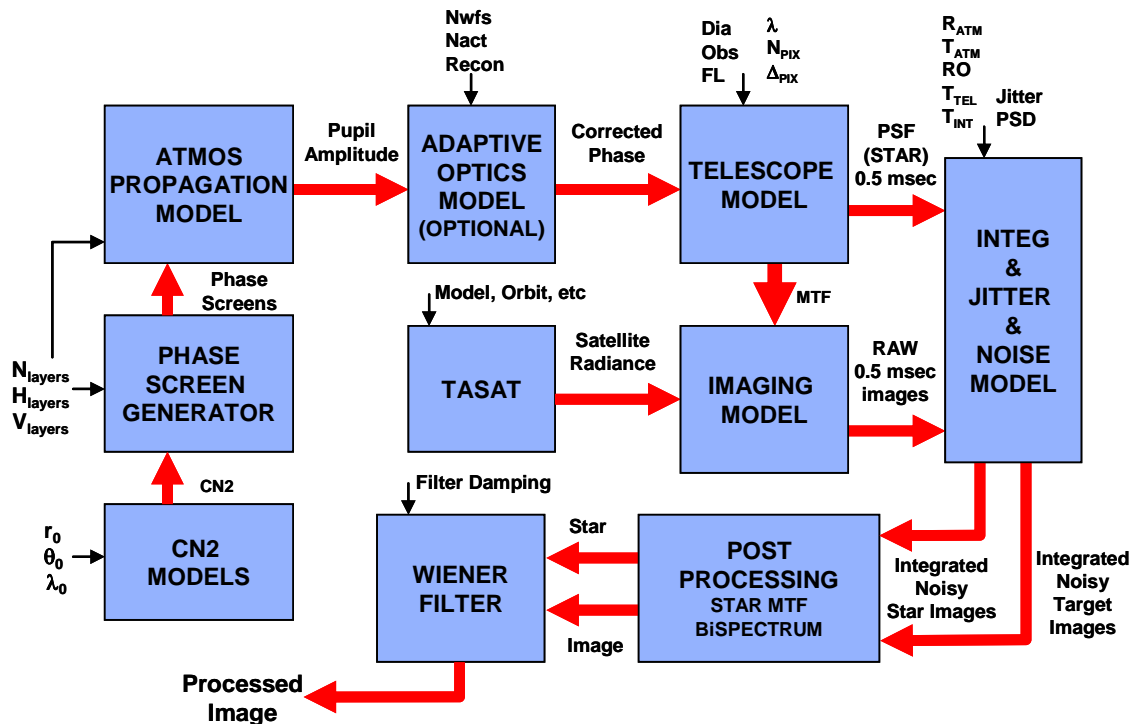


Fig. 3. Detail of the turbulence, optical imaging, and post-processing models

3.1 Orbit profile

The nominal orbit is 450 km altitude sun-synchronous with a 97.2 degree inclination. For the pass used in the simulation, the minimum zenith angle is 45 degrees. Five positions in the orbit were selected having zenith angles of roughly 45, 52.5, and 60 degrees. Fig. 4 shows the track across the sky with the 5 selected positions, and the position of the sun at 10 AM at the site.

3.2 Atmosphere transmission and background

The transmission and background radiance of the atmosphere at the 5 sky positions was calculated with the AFRL-developed PLEXUS code (Phillips Laboratory EXPert-assisted User Software) [1]. Fig. 5 shows the sky radiance at the 45 degree zenith angle, along with the optics transmission and detector quantum efficiency. The view angles, ranges, slew rates, and radiometry for the 5 positions are given in Table 2. The target power and sky background radiance are integrated in-band for the visible and NIR channels.

3.3 Satellite radiance

The satellite radiance signatures were generated using the TASAT code (Time-domain Analysis and Simulation for Advanced Tracking) developed by Northrop-Grumman [2]. High resolution 512x512 pixel images for five positions were generated of the HiFly satellite, which is a hypothetical imaging satellite model delivered with the TASAT software. The radiance profiles for the five positions are shown in Fig. 6. Position 2 is much brighter because of a couple of strong glints which are not obvious in the image of Fig. 6 because of the display scaling.

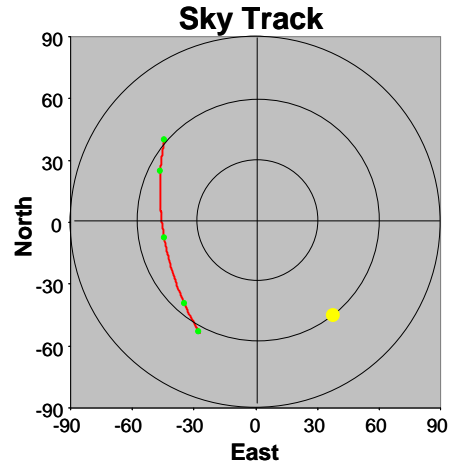


Fig. 4. Track of the satellite across the sky

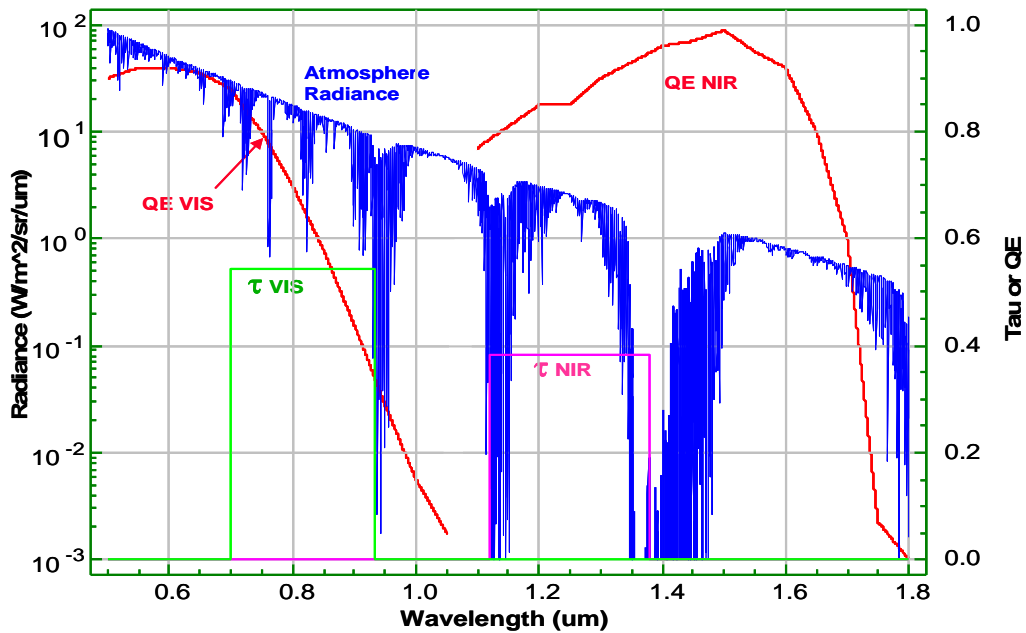


Fig. 5. Atmosphere radiance from Plexus, telescope transmission, and detector quantum efficiency

Table 2. Target parameters at the 5 orbital positions

Pos	Time (sec)	Zenith angle (deg)	Azimuth angle (deg)	Range (km)	Slew rate (rad/sec)	Power in aperture ($W \times 10^{-11}$)		Solar phase (deg)	Background radiance ($W/m^2/sr$)	
						Vis	NIR		Vis	NIR
1	-73	59.8	207.5	818.8	0.0080	3.873	0.465	119.0	2.56	0.301
2	-45	52.5	221.4	699.2	0.0119	37.93	6.047	114.1	1.98	0.227
3	0	45.1	260.2	615.5	0.0177	13.37	1.472	99.0	1.34	0.143
4	+44	52.4	298.0	698.7	0.0119	19.22	2.224	81.8	1.36	0.138
5	+72	59.8	312.0	818.0	0.0081	18.98	2.433	73.7	1.59	0.162



Fig. 6. Satellite radiances obtained with TASAT for the five orbital positions

3.4 Atmosphere turbulence profiles

The “KTL-best” turbulence profile is a modification of the CLEAR1 profile [3] with a 3X stronger boundary layer, adjusted to a ground altitude of 1.621 km instead of 1.230 km, meant to represent 50th percentile good seeing on the WSMR valley floor in the daytime:

$$C_N^2 = \begin{cases} 10^{-10.7025-4.3507(h-0.401)+0.8141(h-0.401)^2} + 3 \times 1.506 \times 10^{-15} e^{-(h-1.621)/0.05} & 1.621 < h < 2.525 \\ 10^{-16.2897+0.0355h-0.0134h^2} & 2.525 < h < 10.342 \\ 10^{-17.0577-0.0449h-0.0005h^2+0.6181 \exp[\frac{1}{2}((h-15.5617)/3.4666)^2]} & h > 10.342 \end{cases} \quad (1)$$

where h is the altitude above sea level, and h_{GND} is 1.621 km at the Kirtland site. This profile gives a Fried parameter r_0 of 7.8 cm at 0.5 μ m, which is moderate seeing. The r_0 is 14.1 cm in the visible band at 0.8175 μ m and 23.5 cm in the NIR band at 1.25 μ m at the 45 degree zenith angle.

The “KTL-worst” profile is a version of the Hufnagel-Valley model [3] with an enhanced boundary layer (HV-B), meant to represent 90th percentile bad seeing on the WSMR valley floor during daytime:

$$C_N^2 = 8.2 \times 10^{-26} (21)^2 h^{10} e^{-h} + 2.7 \times 10^{-16} e^{-(h-h_{GND})/1.5} + 1.7 \times 10^{-14} e^{-(h-h_{GND})/0.1} + 3 \times 1.727 \times 10^{-14} e^{-(h-h_{GND})/0.03} \quad (2)$$

This profile gives a Fried parameter r_0 of 3.2 cm at 0.5 μ m wavelength and 45 degrees, which is fairly bad seeing.

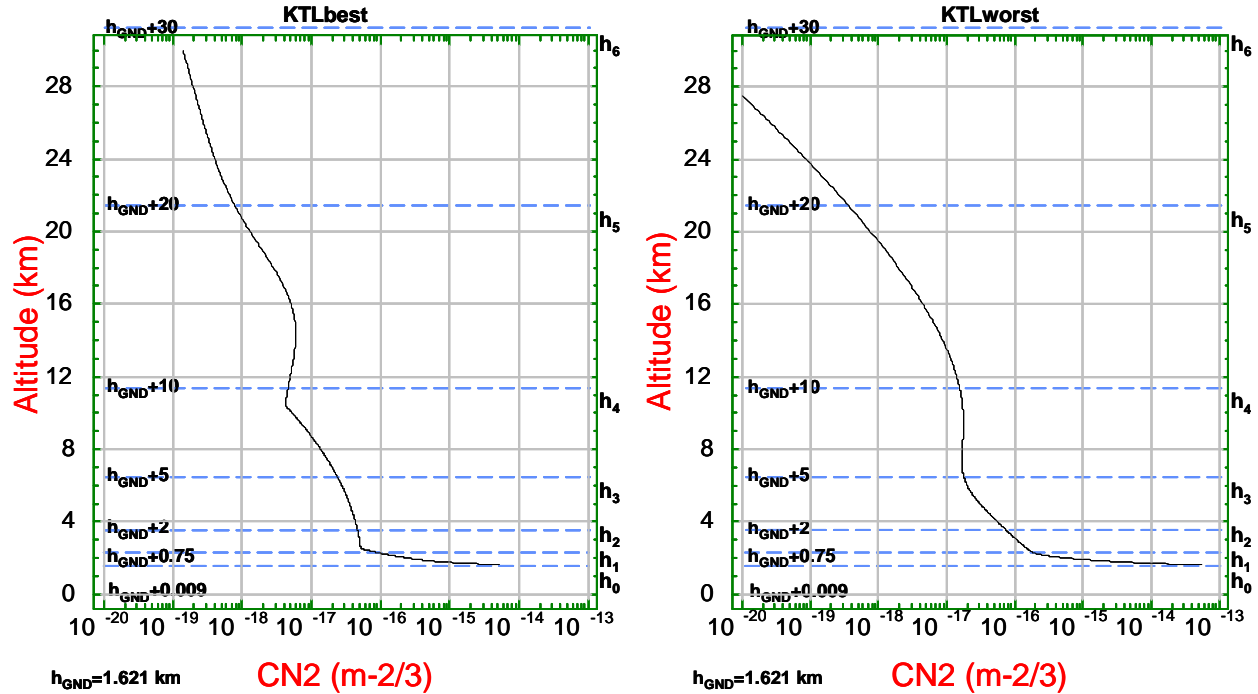


Fig. 7. Atmospheric turbulence CN^2 profiles. Left:KTL-best, right: KTL-worst

The r_0 is 5.8 cm in the visible band and 9.7 cm in the NIR band. The high slew rates give a Greenwood frequency of 230 Hz, for a phase correlation time constant t_0 of 0.69 msec in the visible band (0.8175 μm). This rapidly changing atmosphere drives the sub-millisecond frame sampling in both simulations, even without adaptive optics. Integration is done over the path starting at the telescope aperture, 9 meters above the ground, or $h = 1630$ meters.

3.5 Atmosphere turbulence model

A multilayer propagation algorithm is used to calculate the amplitude and phase of the light from the target impinging on the telescope aperture, with the phase at each layer of the atmosphere generated from the Kolmogorov spectrum of turbulence. In the Aerospace model, the split-step propagation method is used with 6 unequally spaced layers, with an angular spectrum propagation integral [4] performed from the center of one layer to the next. Fig. 8 shows the geometry of the satellite tracking, atmosphere layers, and wind profile.

The spectral density of the phase variations in a layer is specified by the van-Karman form of the Kolmogorov spectrum

$$\Phi_{\phi_j}(f) = \frac{0.023r_{0j}^{-5/3} e^{-f^2/f_m^2}}{(f^2 + f_0^2)^{11/6}} \quad (3)$$

where f is the radial spatial frequency, and f_0 is the low frequency cutoff from the outer scale parameter L_0 . The Fried parameter r_{0j} of the j -th layer is obtained by integrating between the layer boundaries

$$r_{0j} = \left[0.422 \left(\frac{2\pi}{\lambda} \right)^2 \sec^2 \theta_z \int_{h_{j-1}}^{h_j} C_n^2(h) dh \right]^{-3/5} \quad (4)$$

Phase screens are generated by the standard FFT method [5] of filtering 2D arrays of random numbers by the spectrum of the phase in Eq. 3. The ‘‘frozen flow’’ hypothesis is used, assuming that the shape of the phase will not change significantly in the time it takes to move across the telescope aperture, especially given the high slew rates encountered in satellite tracking. Phase screens are generated continuously in any direction by appending random-number arrays to the appropriate side of the original array and filtering again by the turbulence spectrum. The azimuth of the wind speed vector θ_w can be any direction in each of the layers to model wind shear, and the slew azimuth θ_s can be in any direction in the Aerospace model.

It is well known that the FFT method generates turbulence phase spectra that are deficient in low frequencies, particularly tilt. In the Aerospace model this effect was minimized by using phase screens much larger than the telescope aperture (1536x1536 point screens vs. 161 points across the aperture). Also since the bispectrum processing is insensitive to image centroid shifts [6], this deficiency in the tilt will not affect the post-processed images. However, any simulations of the tracking sensor will require an accurate representation of the tilt in the wavefront. A future version of the Aerospace phase-screen generator will correct the low frequency content by adding appropriate amounts of low-order Zernike polynomials with correlation for screen movement.

The velocity vector of a turbulent layer perpendicular to the telescope line of sight is given by

$$\mathbf{V}_l = (V_l \sin \theta_{wl} + \omega_s h_l \sin \theta_s) \hat{\mathbf{x}} + (V_l \cos \theta_{wl} \sin \theta_z + \omega_s h_l \cos \theta_s) \hat{\mathbf{y}} \quad (5)$$

where ω_s is the slew rate, θ_{wl} is the wind direction at the layer, θ_z is the zenith angle, θ_s is the slew direction, and h_l is the layer height. V_l is the wind speed of the layer, here given by the standard Greenwood profile [7]

$$V_l(H_l) = V_G + V_T \exp[-((h_l - h_p)/h_w)^2] \quad (6)$$

where $V_G = 5$ m/s, $V_T = 30$ m/s, $h_p = 9.4$ km, and $h_w = 4.8$ km.

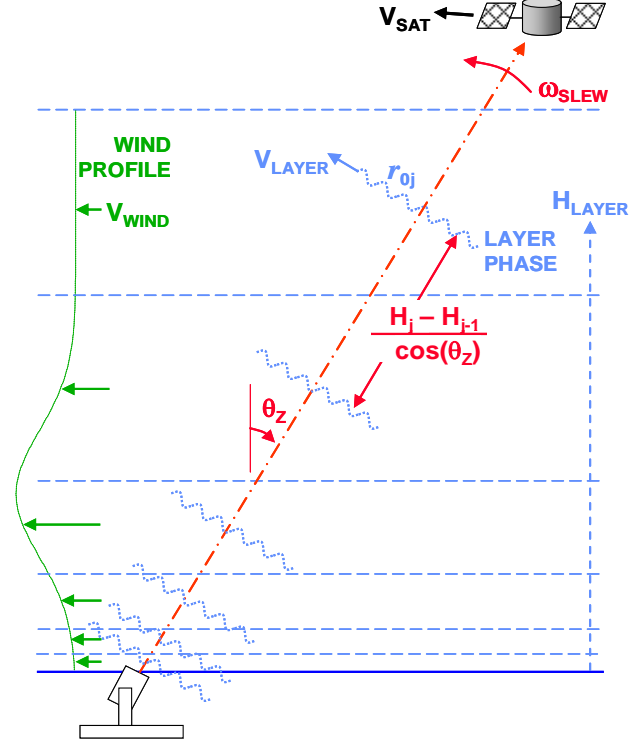


Fig. 8. Multilayer turbulence model

Using the layer position as a function of time, 320x320 point arrays are extracted from the phase screens to sub-pixel shift resolution with a bispectrum interpolation for use in the split-step propagations.

In the Trex model, 10 equally spaced layers are used up to 30 km above the ground, with the option of a simpler and much faster ray-tracing method between the layers, which essentially stacks up the phases in each layer, used for the results presented here. This gives no scintillation in the telescope aperture, but Trex has shown that the resulting phase distribution and images are almost indistinguishable from that obtained with wave propagation for moderate turbulence. A new phase screen is used for each integration time interval, so that the screens are uncorrelated between integration intervals. Also, Trex uses the phase screen generator module from AOTools written by The Optical Sciences Company (tOSC), which can restore the proper amount of tilt to the phase screens.

3.6 Optics and Imaging model

Both imaging models model apply a transfer function to the object spectrum obtained by stacking up a number of Modulation Transfer Function (MTF) components:

$$\tilde{I}(u, v) = \tilde{O}(u, v)H_{ATM}(u, v)H_{OQF}(u, v)H_{JIT}(u, v)H_{DET}(u, v) \quad (7)$$

where $\tilde{O}(u, v)$ is the spectrum of the TASAT radiance image. The various MTF components are

$H_{ATM}(u, v)$ = OTF of telescope+turbulence, from autocorrelation of the complex amplitude in the pupil,

$H_{OQF}(u, v) = 1 + [1 - \exp(-4\pi^2\sigma^2/\lambda^2)][\exp(-u\lambda f/\rho D) - 1]$ is a telescope optical quality MTF,

$H_{DET}(u, v) = \text{sinc}(uW_x, vW_y)$ is the detector pixel MTF, width W_x, W_y ,

$H_{JIT}(u, v) = \exp[-2\pi^2\sigma_j^2(u^2 + v^2)]$ Gaussian jitter of telescope, σ_j is the standard deviation.

These MTF components are resampled to the frequency increment of the object spectrum by a bilinear interpolation. For the telescope quality factor we used wavefront error $\sigma = 0.142 \mu\text{m rms}$, and correlation length $\rho = D/5$. D and f are the diameter and focal length respectively. The jitter MTF is an inter-frame jitter, i.e., blur occurring during an integration time. In the Aerospace model, intra-frame jitter can also be modeled by sampling a time series of jitter generated with a given power spectral density, and shifting each 0.5 sub-frame image with a phase ramp in the MTF. The image is then resampled to the pixel locations using an algorithm based on the Fourier integral, not an FFT:

$$I(j\Delta x, k\Delta y) = \iint \tilde{I}(u, v) \exp 2\pi(j\Delta x u + k\Delta y v) du dv \quad (8)$$

The Trex algorithm first downsamples the TASAT radiance to the Nyquist grid with averaging over the effective pixel IFOV, then carries this sampling all the way through the propagation and image formation using the FFT. Jitter is modeled as a Gaussian-distributed sampled time series in the sub-frames.

3.7 Bispectrum post-processing

The bispectrum is a speckle-imaging algorithm which recovers the phase of an image spectrum from multiple images degraded by turbulence. Details of the bispectrum algorithm will not given here; for a description see [6]. Aerospace obtained a bispectrum algorithm developed by C. Matson of AFRL, written in Fortran for LINUX [8]. Trex used an algorithm implemented in MATLAB by Michael Roggemann of Michigan Technological University.

Since the bispectrum calculates only the phase of the object spectrum, the amplitude is degraded by the average MTF of the turbulence. To correct for this, we first need to estimate the short-term average MTF of the atmosphere from images of a reference star, using the same integration time:

$$\tilde{H}_{REF}(u, v) = \left[\frac{1}{N} \sum_j |\tilde{I}_{STAR,j}(u, v)|^2 \right]^{1/2} \quad (9)$$

and then deconvolve this from the output of the bispectrum to get the final post-processed image of the target. We use a normalized Wiener filter

$$\hat{I}(x, y) = FT^{-1} \left[\frac{\tilde{I}_{BS}(u, v) \tilde{H}_{REF}^*(u, v) (1 + \alpha^2(0,0))}{|\tilde{H}_{REF}(u, v)|^2 + \alpha^2(u, v)} \right] \quad (10)$$

where the regularization parameter α in theory should be the noise/signal ratio as a function of frequency; here we implement it as a small constant, usually 0.01 – 0.001. Even though the star slew rate is much slower, and thus the temporal bandwidth of the turbulence is much lower, the resulting reference MTF gives good results for the deconvolution. More frames of star images are needed to get good averaging of the MTF, however.

3.8 Summary of model features and differences

The main differences in the implementations of the simulation by Trex and Aerospace are in the atmospheric turbulence model and the optical imaging model. The salient features and differences are shown in Table 3. PHOCAS (PHysical Optics Code for Analysis and Simulation) is a wave-propagation and optical analysis code developed by R. Boucher at The Aerospace Corporation.

Table 3. Model features and differences

Aerospace Model	TREX Model
Developed with in-house code (PHOCAS) FFT screen generation, 1536x1536 points Continuous screen generation for wind and slew in any direction for each layer for full 2 seconds 6 unequally-spaced layers with boundaries at 0.75, 2, 5, 10, 20, 30 km above ground Split-step wave propagation between layers. Gives scintillation in telescope aperture. 320x320 point phase screens extracted for split-step propagation using a bilinear interpolation 161 points across telescope aperture 0.5 msec subframes x 40 subframes for 20 msec Downsample to pixels in frequency domain Bispectrum from C. Matson, in LINUX Fortran [8]	Developed in-house with MATLAB FFT screen generation with added tilt, uses tOSC phase AOTools screen generator, 1024x1024 points Uncorrelated phase screens generated for each integration time, moving during the integration only 10 equally-spaced layers up to 30 km above ground Split-step or raytracing between layers, i.e. phase stacking. No scintillation latter case. 256x256 point phase screens extracted to pixel resolution without interpolation 256 points across telescope aperture 0.25 msec sub-frames x 80 sub-frames for 20 msec Downsample to pixels in spatial domain Bispectrum from M. Roggemann, in MATLAB [6]

4. SIMULATION RESULTS

Simulations were run for all 5 satellite positions, visible and NIR channels, with the best and worst atmospheres, and in addition various excursions were performed on telescope diameter, Wiener filter parameter, and object brightness, but only a very few results can be shown here. Figs. 9-12 were generated using the Aerospace model.

For the moderate atmosphere, KTL-best, fairly good results were obtained. Fig. 9 shows a sample turbulence-degraded image, along with the processed image compared to the diffraction-limited image for position 3 in the visible camera. The image is close to diffraction-limited quality, with a moderate amount of noise, and has a high potential for accurate determination of satellite attitude. However, position 1, in Fig. 10, gives a poor reconstruction because the lower radiance does not provide adequate signal to noise for the bispectrum algorithm.

Simulations with the severe atmosphere, KTL-worst, in general generated very poor reconstructions that would be inadequate for attitude determination. A sample result is shown in Fig. 11 for position 3. The most likely reason for the failure is that the stronger turbulence significantly reduces the signal-to-noise ratio of the acquired images.

In the near-IR, simulations with the moderate atmosphere also gave fairly good results, as shown in Fig. 12. The image is close to diffraction limited, and seems less noisy, although the resolution is lower at the longer wavelength.

Comparisons of the images generated by the Aerospace and Trex models in the visible for the two turbulence cases are shown in Fig. 13 and 14. Despite what may seem to be marked differences in the implementations of the turbulence propagation and imaging algorithms, the results are almost indistinguishable in quality. The fringing artifacts in positions 4 and 5 are characteristic of the bispectrum algorithm, and the small differences may be due to the details of the bispectrum implementation and internal SNR thresholds.

5. CONCLUSIONS

The system should perform adequately in conditions of moderate turbulence to obtain a reasonably accurate estimate of the attitude over a sufficient portion of the orbit. In severe turbulence however, the images appear to be unusable for attitude determination with post processing only, and additional exploration need to be done to see if this can be remedied with adaptive optics. Even with what may be considered significant differences in the implementations of the two versions of the models, the post-processed results are very similar. This seems to indicate that phase in the telescope aperture due to atmospheric turbulence is of primary importance, and that the amplitude variation or scintillation derived from a more rigorous wave propagation between the layers has little impact on the final processed image. Simplified and faster models can be used to perform trade studies over a number of parameters to support system design, resorting to more rigorous models for a much smaller set of key cases.

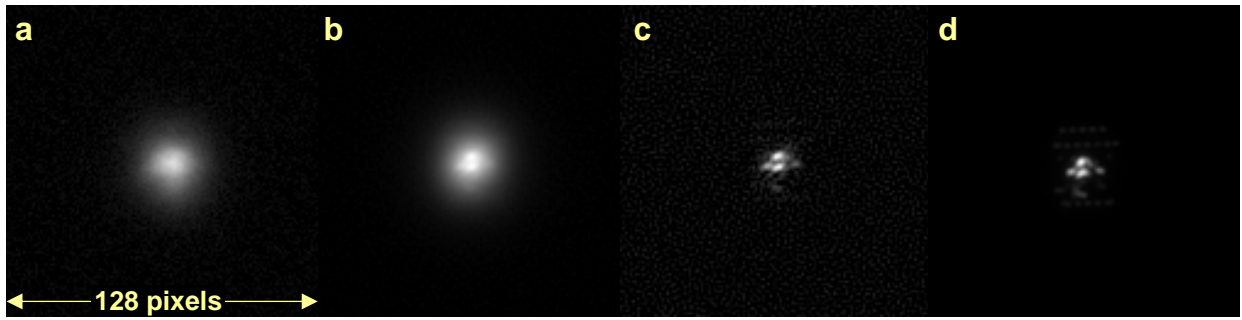


Fig. 9. Simulation outputs for visible, position 3, KTL-best atmosphere. a) raw turbulence degraded frame b) bispectrum output, c) bispectrum output deconvolved with star, d) diffraction-limited image.

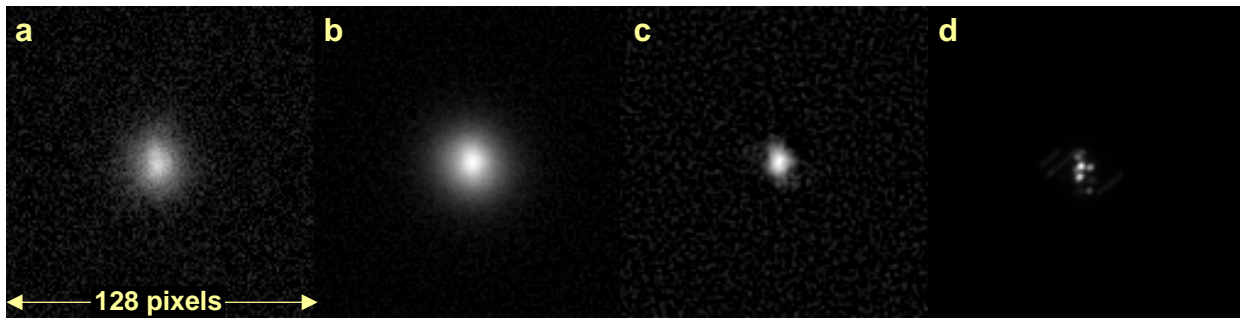


Fig. 10. Simulation outputs for visible, position 1, KTL-best atmosphere. a) raw turbulence degraded frame b) bispectrum output, c) bispectrum output deconvolved with star, d) diffraction-limited image

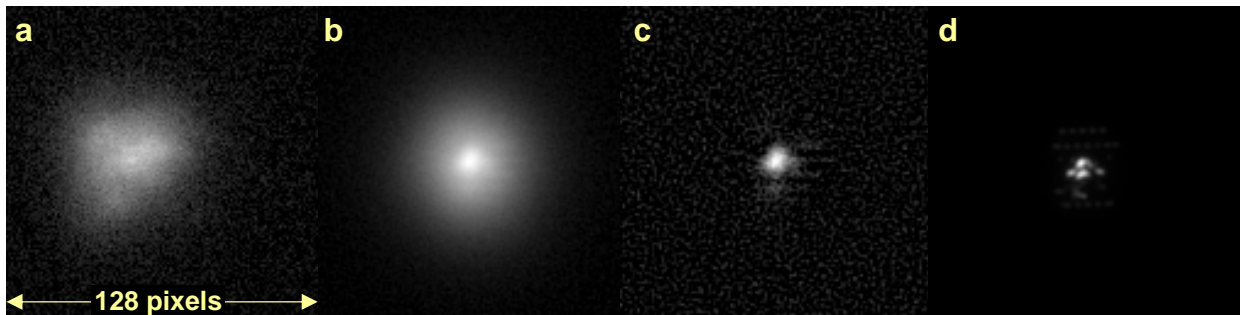


Fig. 11. Simulation outputs for visible, position 3, KTL-worst atmosphere. a) raw turbulence degraded frame b) bispectrum output, c) bispectrum output deconvolved with star, d) diffraction-limited image

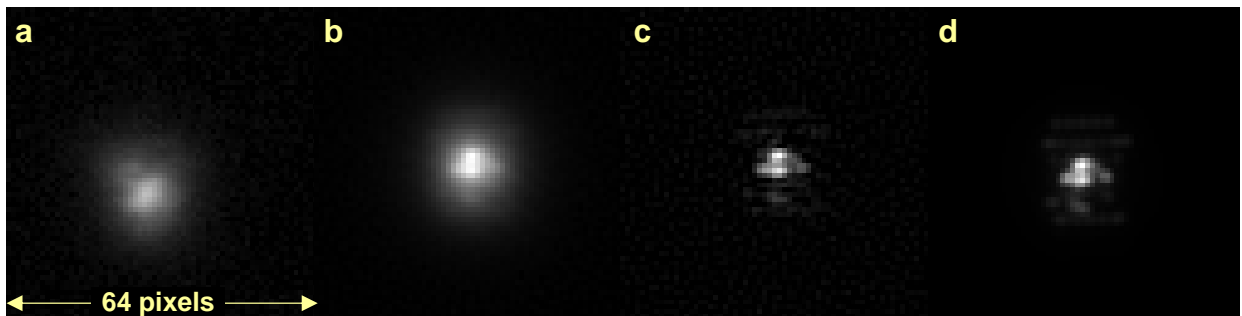


Fig. 12. Simulation outputs for infrared, position 3, KTL-best atmosphere. a) raw turbulence degraded frame b) bispectrum output, c) bispectrum output deconvolved with star, d) diffraction-limited image

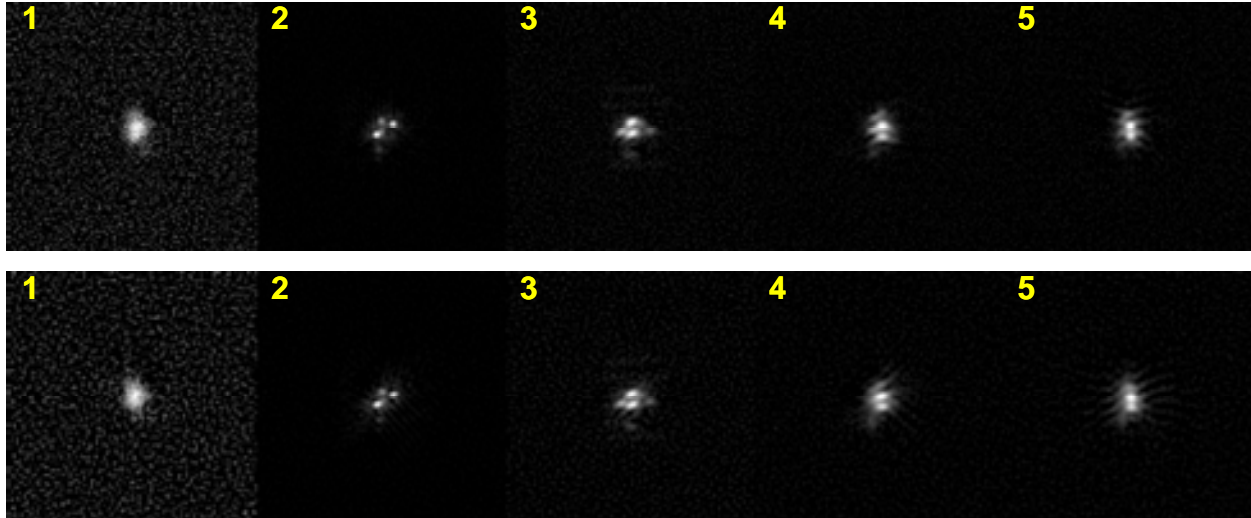


Fig. 13. Outputs of bispectrum processing for the Visible, KTL-best atmosphere. Top: Trex, Bottom: Aerospace

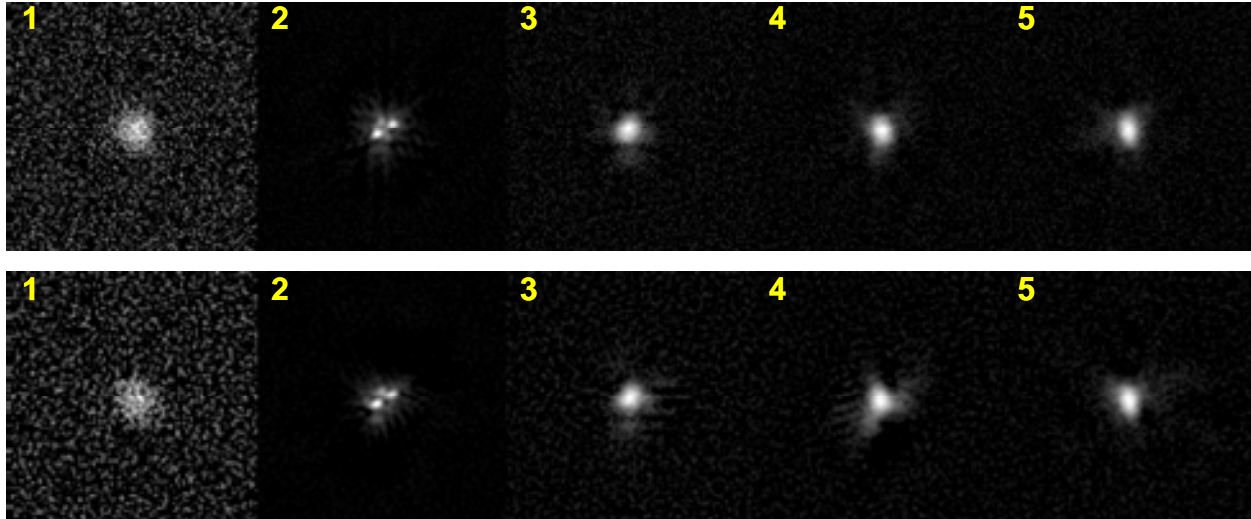


Fig. 14. Outputs of bispectrum processing for the Visible, KTL-worst atmosphere. Top: Trex, Bottom: Aerospace

6. REFERENCES

1. PLEXUS, Phillips Laboratory Expert-assisted User Software, Release 3 Version 3 Beta 1, AFRL, NM, 2006.
2. TASAT, "Time-domain Analysis and Simulation for Advanced Tracking", Northrop Grumman Corp., 2600 Yale Blvd, Albuquerque NM 87106
3. F. Smith, Editor, *The Infrared & Electro-optical Systems Handbook, Volume 2, Atmospheric Propagation of Radiation*, Chapter 2, SPIE Press, Bellingham WA, 1993.
4. Goodman, J.W., *Introduction to Fourier Optics*, McGraw Hill, New York, 1968
5. Johansson, E.M. and Gavel, D.T., "Simulations of stellar speckle imaging", *SPIE Proceedings* Vol. 2200, p. 372
6. Roggemann, M.C. and Welsh, B.M., *Imaging Through Turbulence*, CRC Press, New York, 1996
7. Greenwood, D. P., "Bandwidth specification for adaptive imaging systems", *J. Opt. Soc. Am.* 67, p. 390, 1977
8. Matson, C.L., "Weighted-least-squares phase reconstruction from the bispectrum", *J. Opt. Soc. Am. A* 8, p. 1905.

All trademarks, service marks, and trade names are the property of their respective owners.

The authors wish to thank George L. Clark, Jr., Capt. Ryan McGuire, and Maj. Jonathan Bishop for essential guidance, and Michael C. Roggemann for helpful conversations. This work was supported by the US Air Force Space and Missile Systems Center (SMC) and The Aerospace Corporation's Independent Research and Development Program.